Electronic Supplementary Material (ESI) for Lab on a Chip.

Supporting information

for

Non-contact monitoring of extra-cellular field potentials with a multi-electrode array

by Tal Sharf, Paul K. Hansma, Mukund A. Hari and Kenneth S. Kosik*

*talsharf@ucsb.edu

A. Representative extra-cellular field potential waveforms from non-contact measurements

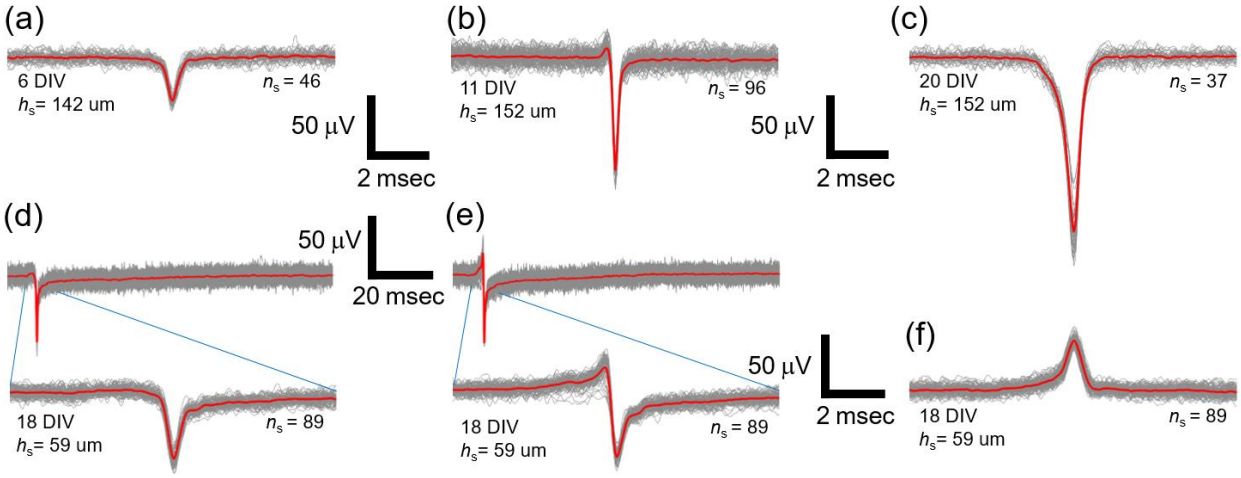

Figure S1. (a-f) Representative extra-cellular field potential waveforms recorded from a multi-electrode array (MEA) in the non-contact configuration from N =10 primary cardiomyocyte culture preparations grown on glass coverslips. Spike triggered averages appear as the red solid line (averaged over the number of detected spikes, n_s, above background noise levels). Individual spike waveforms are plotted in gray. A total of 135 electrodes (from N = 10 preparations) registered spikes distinguishable above background noise: 30 percent of these spikes displayed only negative peaks, 44% displayed an initial positive component followed by negative peak and 26% registered only a positive component to the waveform.

B. Representative extra-cellular field potenial waveforms from cells grown on the surface of a multi-electrode array

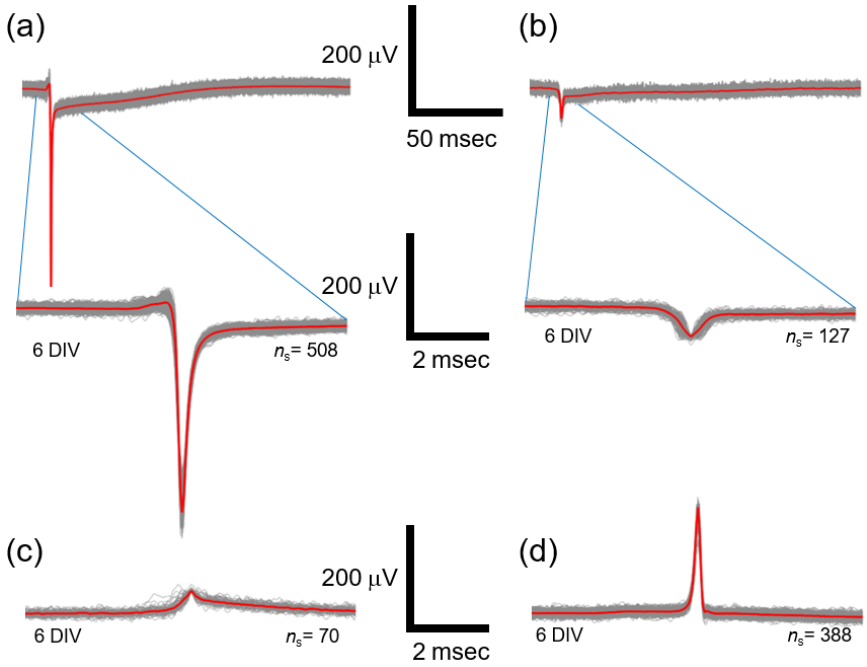

Figure S2. (a-d) Representative extra-cellular field potential waveforms produced by primary cardiomyocyte cells grown on the surface of a multi-electrode array (MEA).

C. Characterization of coverslip surface approach

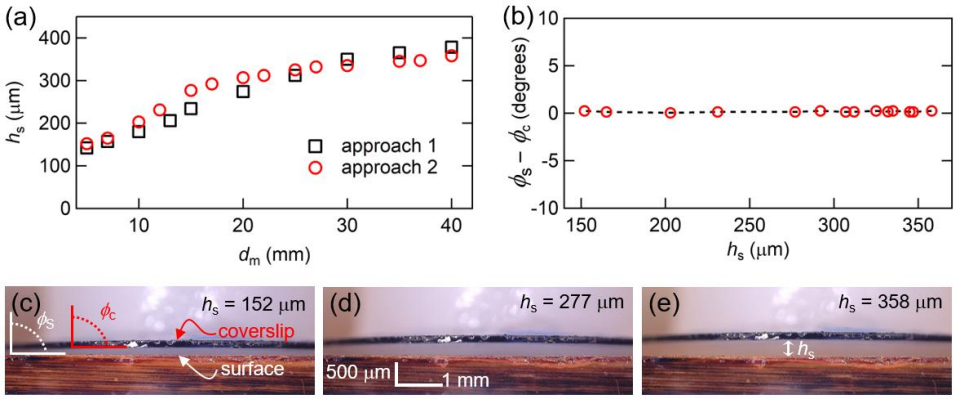

Figure S3. (a) Separate measurements of the coverslip surface height h_s as a function of magnet-magnet separation distance d_m. (b) The relative angular variation between the surface ϕ_s and the coverslip ϕ_c is plotted for fixed coverslip surface heights h_s during approach. The mean angular variation is 0.17° ± 0.06° measured over a distance of 2 mm. The variation in h_s due to angular variability during approach is ≈ 3 μm across the 1.1 mm distance of the recording surface of the multi-electrode array. (c-e) Optical images of the relative coverslip surface height h_s during approach.

D. Microscopy of primary cardiomyocyte cultures

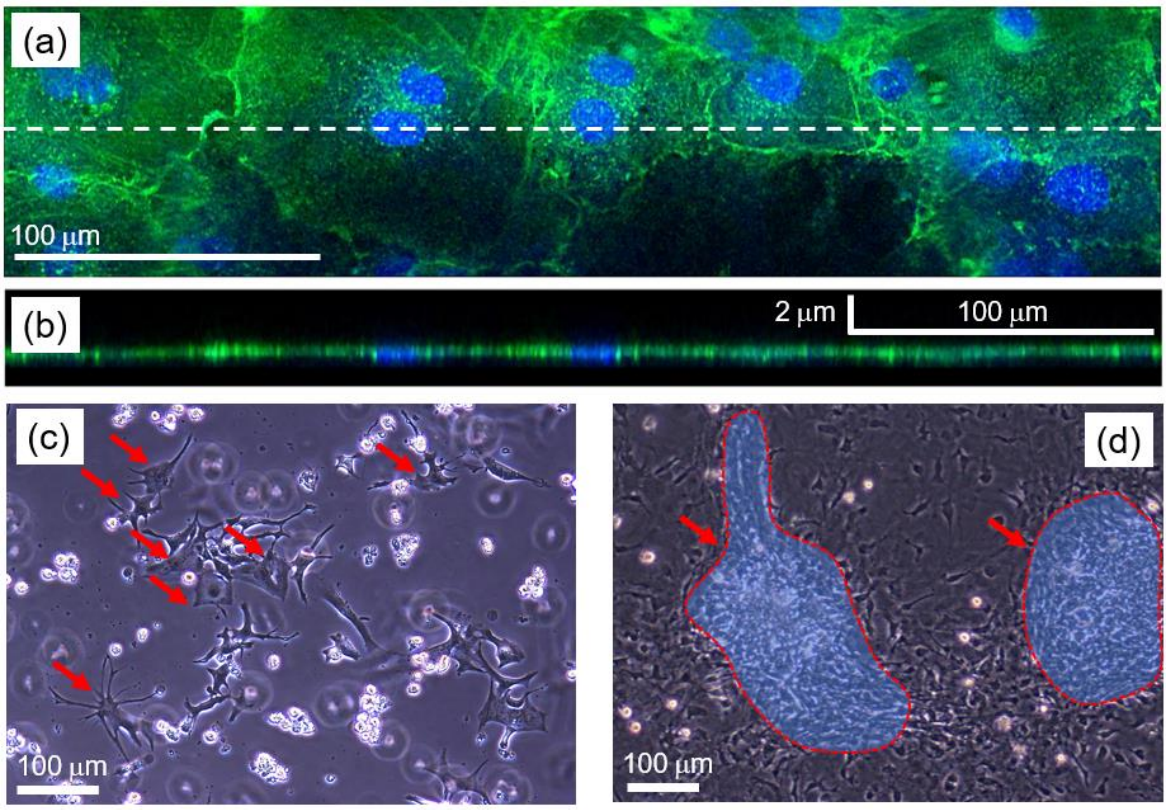

Figure S4. (a) Immunofluorescence images taken of primary cardiomyocyte cultures at 10 *days in vitro* taken with a Leica SP8 resonant scanning confocal microscope using a 63x oil immersion objective. The cell membrane shown in green (WGA-AF488) and nuclei shown in blue (DAPI). The scale bar is 100 μm. (b) Z-stack image taken along the dotted line of (a). The vertical and horizontal scale bars are 2 μm and 100 μm, respectively. (c) Phase contrast images of primary cardiomyocytes cultures taken at 5 days *in vitro*. The red arrows indicate spontaneously contracting cells. The scale bar is 100 μm. (d) Phase contrast images of primary cultures taken at 14 days *in vitro*. The red arrows point to spontaneously contracting, multi-cellular populations and highlighted by the dashed line. The scale bar is 100 μm.

E. Modeling extra-cellular field potentials

The extra-cellular voltage produced by an action potential has been previously shown by Gold *et al.*[1] to be well modeled as an isotropic volume conductor with a purely Ohmic response over a frequency range of interest between 1-3,000 Hz (capacitive effects of the extra-cellular medium are negligible). Under steady-state conditions, the electric potential V_s generated by a point current source I_s flowing through an isotropic volume conductor with electrical conductivity σ is given by

$$V_s = \frac{I_s}{4\pi\sigma \cdot r}, \quad (1)$$

where r the radial distance from the point source.[2]

Cardiomyocyte cultures grow in confluent clusters with ion channels (current sources) spread out across their surfaces. We next approximate the cell clusters as a homogeneous distribution of current sources with current density j_0 distributed across the surface area of a planar 2d disk of radius R_0 as shown by Diagram 1. The contribution of source current, dI_s, at disc radius a is given by $dI_s = j_0 \cdot 2\pi a \cdot da$. The resultant field at point P is the linear superposition of point sources[3] and is given by

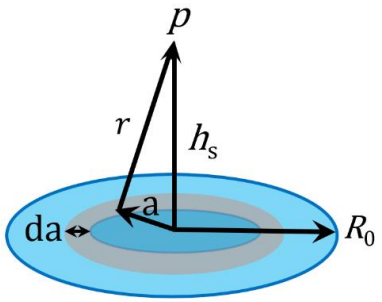

Diagram 1. 2D model of a planar current source in an isotropic volume conductor.

$$V^{theory} = 2 \cdot \int_0^{R_0} \frac{dI_s}{4\pi\sigma \cdot r} = \int_0^{R_0} \frac{j_0 \cdot 2\pi a \cdot da}{4\pi\sigma\sqrt{{h_s}^2 + a^2}} = \frac{j_0}{\sigma}\left(\sqrt{{h_s}^2 + {R_0}^2} - |h_s|\right) + V_0, \quad (2)$$

where h_s is the height from the center of the disk. The extra-cellular voltage is multiplied by a factor of two because current flow subtends half the solid angle for a planar 2D cell culture. The constant V_0 term is added to account for a voltage drop across the recording electrode interface due to finite impedance, as well as any electrochemical voltage offsets due to grounding the liquid. The cell culture media conductivity σ has a value of 1.7 S·m^{-1} at 37 °C.[4] To account for the uncertainty in V_0, we take the derivative of Eq.2 with respect to h_s and arrive at the following expression for the current density

$$j_0 = \sigma\left(\frac{dV}{dh_s}\right) \cdot \left(h_s / \sqrt{{h_s}^2 + {R_0}^2} - 1\right)^{-1}. \quad (3)$$

Note that j_0 depends only the slope (dV/dh_s), determined by the fit to experimental data, and distance h_s for a given culture size set by R_0. This value is independent of the magnitude of the voltage signal, which can vary significantly based on the quality of the recording electrode.[5]

Figure S5a,b shows the experimentally measured extra-cellular field potential vs. time for various surface heights h_s from the recording surface of a MEA. Figure S5c shows V^{theory} as a function of height h_s from the cell-culture surface, for R_0 = 150 μm and j_0 = 1.7 A/m^2. The red circles and black diamonds, shown in Figure S5d, indicate experimentally measured maximum voltage amplitudes (extracted from Figure S5a,b) measured at 6 DIV (V_6^{expt}) and 18 DIV (V_{18}^{expt}). The dotted lines are theoretical fits V_6^{theory} and V_{18}^{theory} to the experimental data using Eq.2. A two-parameter fit was used to determine j_0 and V_0 for a fixed excitable culture area set by R_0. The excitable area was determined by spatial distribution of synchronized spiking activity measured by the MEA. Cardiomyocyte activation travels as a wave of electrical activity which propagates from cell-to-cell with an average velocity of ≈ 0.3 m·s^{-1}.[6–8] Voltage signals detected at a given electrode on the MEA are the superposition of all synchronized extra-cellular field

potentials. For a fixed reference point, extra-cellular field potential signals are additive over a maximum spatial window of ≈ 300 µm assuming a depolarization time of ≈ 0.5 ms, therefore we used an R_0 =150 µm. We find j_0 = 1.7 A·m^{-2} and 2.4 A·m^{-2} for the 6 and 18 DIV respectively. These results are consistent with whole-cell patch-clamp measurements that give current densities of around ≈ 1-3 A·m^{-2} (The magnitude of whole cell transmembrane currents span the range 10^{-9} A to 10^{-8} A,[9–12] which flow across an area of ≈ $4\cdot10^{-9}$ m^2.[6,12,13]).

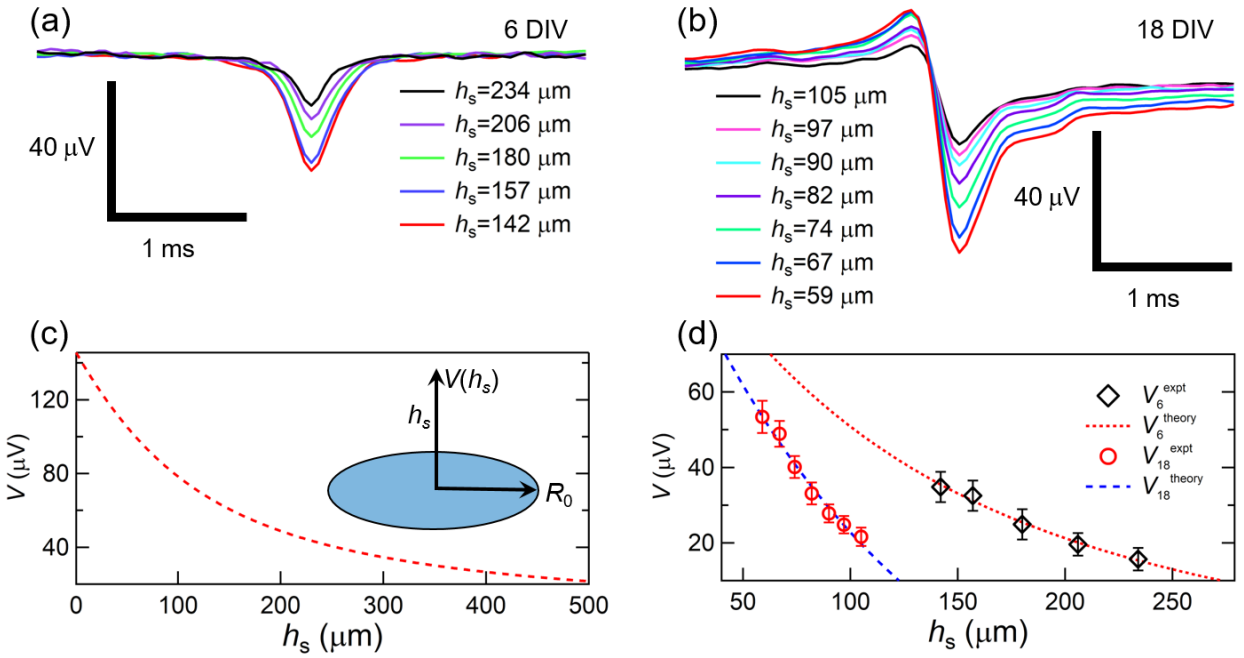

Figure S5. Distance dependence of extra-cellular field potentials. (a-b) Experimental non-contact measurements of extra-cellular field potentials from cardiomyocyte cultures at 6 *days in vitro* (DIV) and 18 DIV for various separation heights from the surface of a multi-electrode array. The voltage vs. time plots are the spike triggered average waveforms. (c) Theoretically modeled extra-cellular voltage as a function a distance h_s from the cell surface. (d) Experimentally measured extra-cellular peak voltage amplitude as a function of distance for two representative cardiomyocyte cultures at 6 DIV (V_6^{expt}, black diamonds) and 18 DIV (V_{18}^{expt}, red circles). The dashed lines are theoretical fits to the data.

The parameters of our model-dependent results assume homogenous spatial distribution of the cells, which is a reasonable approximation for the contiguous arrangements of cardiomyocytes whose temporal activation is synchronized via gap-junctions.[6] Incorporating cell patterning techniques would help to define more precise spatial geometries of varying degrees of complexity, ranging from sculpting the shape of single cells[14] to templating the geometry of large populations that direct information flow through out interconnected networks.[15–17] Lastly, combining these techniques with high-channel count MEAs[18–20] would enable the development of more precise

computational models used to describe extra-cellular fields generated by inhomogeneous spatial configurations.

1 C. Gold, D. A. Henze, C. Koch and G. Buzsáki, *J Neurophysiol*, 2006, **95**, 3113–3128.

2 P. L. Nunez and R. Srinivasan, *Electric Fields of the Brain: The neurophysics of EEG*, 2009.

3 J. D. Jackson, *Classical Electrodynamics*, Third Edit., 1998.

4 A. P. Mazzoleni, B. F. Sisken and R. L. Kahler, *Bioelectromagnetics*, 1986, **7**, 95–99.

5 S. Suner, M. R. Fellows, C. Vargas-Irwin, G. K. Nakata and J. P. Donoghue, *IEEE Trans. Neural Syst. Rehabil. Eng.*, 2005, **13**, 524–541.

6 M. S. Spach, J. F. Heidlage, P. C. Dolber and R. C. Barr, *Circ. Res.*, 2000, **86**, 302–311.

7 A. Natarajan, M. Stancescu, V. Dhir, C. Armstrong, F. Sommerhage, J. J. Hickman and P. Molnar, *Biomaterials*, 2011, **32**, 4267–4274.

8 G. Meiry, Y. Reisner, Y. Feld, S. Goldberg, M. Rosen, N. Ziv and O. Binah, *J. Cardiovasc. Electrophysiol.*, 2001, **12**, 1269–1277.

9 S. Fredj, K. J. Sampson, H. Liu and R. S. Kass, *Br. J. Pharmacol.*, 2006, **148**, 16–24.

10 M. P. Davies, R. H. An, P. Doevendans, S. Kubalak, K. R. Chien and R. S. Kass, *Circ Res*, 1996, **78**, 15–25.

11 M. Mille, X. Koenig, E. Zebedin, P. Uhrin, R. Cervenka, H. Todt and K. Hilber, *Pflugers Arch. Eur. J. Physiol.*, 2009, **457**, 1023–1033.

12 L. Formigli, F. Francini, S. Nistri, M. Margheri, G. Luciani, F. Naro, J. D. Silvertown, S. Z. Orlandini, E. Meacci and D. Bani, *J. Mol. Cell. Cardiol.*, 2009, **47**, 335–345.

13 M. A. Crackower, G. Y. Oudit, I. Kozieradzki, R. Sarao, H. Sun, T. Sasaki, E. Hirsch, A. Suzuki, T. Shioi, J. Irie-Sasaki, R. Sah, H. Y. M. Cheng, V. O. Rybin, G. Lembo, L. Fratta, A. J. Oliveira-dos-Santos, J. L. Benovic, C. R. Kahn, S. Izumo, S. F. Steinberg, M. P. Wymann, P. H. Backx and J. M. Penninger, *Cell*, 2002, **110**, 737–749.

14 F. Patolsky, B. P. Timko, G. Yu, Y. Fang, A. B. Greytak, G. Zheng and C. M. Lieber, *Science*, 2006, **313**, 1100–1104.

15 B. C. Wheeler and G. J. Brewer, *Proc. IEEE*, 2010, **98**, 398–406.

16 S. Dauth, B. M. Maoz, S. P. Sheehy, M. A. Hemphill, T. Murty, M. K. Macedonia, A. M. Greer, B. Budnik and K. K. Parker, *J. Neurophysiol.*, 2017, **117**, 1320–1341.

17 O. Feinerman, A. Rotem and E. Moses, *Nat. Phys.*, 2008, **4**, 967–973.

18 D. J. Bakkum, U. Frey, M. Radivojevic, T. L. Russell, J. Müller, M. Fiscella, H. Takahashi and A. Hierlemann, *Nat. Commun.*, 2013, **4**, 2181.

19 J. Müller, M. Ballini, P. Livi, Y. Chen, M. Radivojevic, A. Shadmani, V. Viswam, I. L. Jones, M. Fiscella, R. Diggelmann, A. Stettler, U. Frey, D. J. Bakkum and A. Hierlemann, *Lab Chip*, 2015, **15**, 2767–2780.

20 D. Jäckel, D. J. Bakkum, T. L. Russell, J. Müller, M. Radivojevic, U. Frey, F. Franke and A. Hierlemann, *Sci. Rep.*, 2017, **7**, 978.